

Controlling nanoslot overlimiting current with the depth of a connecting microchamber

This article has been downloaded from IOPscience. Please scroll down to see the full text article.

2010 EPL 90 64004

(<http://iopscience.iop.org/0295-5075/90/6/64004>)

View [the table of contents for this issue](#), or go to the [journal homepage](#) for more

Download details:

IP Address: 129.74.250.206

The article was downloaded on 16/11/2010 at 01:32

Please note that [terms and conditions apply](#).

Controlling nanoslot overlimiting current with the depth of a connecting microchamber

G. YOSSIFON^{1(a)}, P. MUSHENHEIM² and H.-C. CHANG²

¹ Faculty of Mechanical Engineering, Micro- and Nanofluidics Laboratory, Technion - Israel Institute of Technology - Technion City 32000, Israel

² Department of Chemical and Biomolecular Engineering, Center for Microfluidics and Medical Diagnostics, University of Notre Dame - Notre Dame, IN 46556, USA

received 30 March 2010; accepted in final form 9 June 2010
published online 13 July 2010

PACS 47.61.Fg – Flows in micro-electromechanical systems (MEMS) and nano-electromechanical systems (NEMS)

PACS 47.57.jd – Electrokinetic effects

PACS 82.39.Wj – Ion exchange, dialysis, osmosis, electro-osmosis, membrane processes

Abstract – The overlimiting ion flux, in excess of the limiting-value stipulated by diffusion, across a wide nanoslot (of fixed depth) is shown to be sensitively dependent on the depth of the connecting microchamber at one end of the nanoslot, which controls the onset of a vortex instability that specifies the dimension of the concentration polarization layer responsible for overlimiting behavior. Simple scaling arguments relating the microchamber depth to the effective fluid viscosity produce experimentally verified scaling dependence of the polarization layer length, the onset voltage for overlimiting behavior and the overlimiting current on the microchamber depth.

Copyright © EPLA, 2010

In recent years, fabrication of ion-selective nanochannels with overlapping double layers has produced simple single-pore chip models (*e.g.*, fig. 1) of ion-selective nanoporous membranes or biological ion channels on cell membranes. As a result, the nonlinear ion transport [1] and the resulting ion-enrichment/depletion [2], overlimiting current [3] and ionic current rectification [4,5] phenomena can be examined to reveal the mechanisms behind many curious nonlinear current-voltage (I - V) behavior of ion-selective membranes. This effort could lead to smart designs of ion-selective membranes for desalination, molecular sieving, artificial cells, solar cells etc, as well as sensitive electrode sensors [6].

An important and yet relatively unexplored I - V characteristic of conducting ion-selective membranes and fabricated nanochannels of fig. 1 is that, at sufficiently high voltages, its current density often exceeds the limiting current density predicted by the classical diffusion-limited current transport theory [7]. At the limiting-current condition, a neutral diffusion layer (DL), with a concentration profile that increases monotonically from nearly zero and with a voltage-independent ion flux, extends from the

electric Debye layer (EDL) of the nanochannel depleted entrance to either the electrode or to a well-mixed region without concentration gradient. Later theories by Rubinstein and Shtilman [8] suggest that, at higher voltages, an extended polarized layer (or space charge layer —SCL), much larger than the Debye length λ , can appear between the EDL and the electro-neutral DL to precipitate an electroconvection instability that sustains an overlimiting current, which can be significantly higher than the limiting current and even with a lower differential resistance than the ohmic value (fig. 2(a)). These three different layers are collectively termed the concentration polarization layer (CPL). This new overlimiting region, with ion fluxes much higher than the limit imposed by diffusion, is extremely attractive for many ion-selective membrane (*e.g.* solar cell) and bio-sensor (electron-transfer) applications.

As was verified by earlier experiments [9,10], the mechanism for selecting the CPL thickness L is through the electroconvection instability of the SCL. The onset of the instability is controlled by an overvoltage wherein the overlimiting region associated with this instability appears only beyond a critical voltage. This instability develops into a stationary vortex array on the depleted

^(a)E-mail: yossifon@tx.technion.ac.il

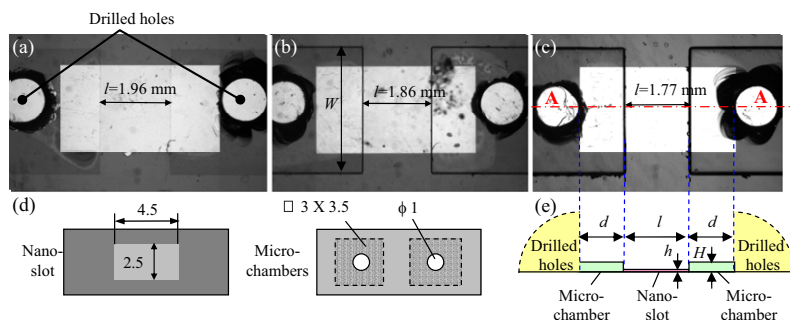


Fig. 1: (Color online) Microscopy images of the chips (top views) with a constant nanoslot height ($h = 190$ nm) and varying microchamber heights (a) $2 \mu\text{m}$, (b) $44 \mu\text{m}$ and (c) $122 \mu\text{m}$. Overetching resulted in decreasing nanoslot length (l) with increased microchamber height; (d) schematic of the two Pyrex slides (top view) making the chip. Left slide —rectangle of 2.5 mm width and 190 nm depth, that is etched into the deposited polysilicon layer on top of a Pyrex glass slide. Right slide —two square microchambers that were wet-etched into a second Pyrex glass slide. Inlet/outlet access holes were mechanically drilled into the center of each microchamber. Sealing of these two glass slides form the nanoslot that connects the two microchambers; (e) schematic (side-view cross-section A-A) of the chip geometry wherein the microchambers of controlled depth are truncated by the drilled holes.

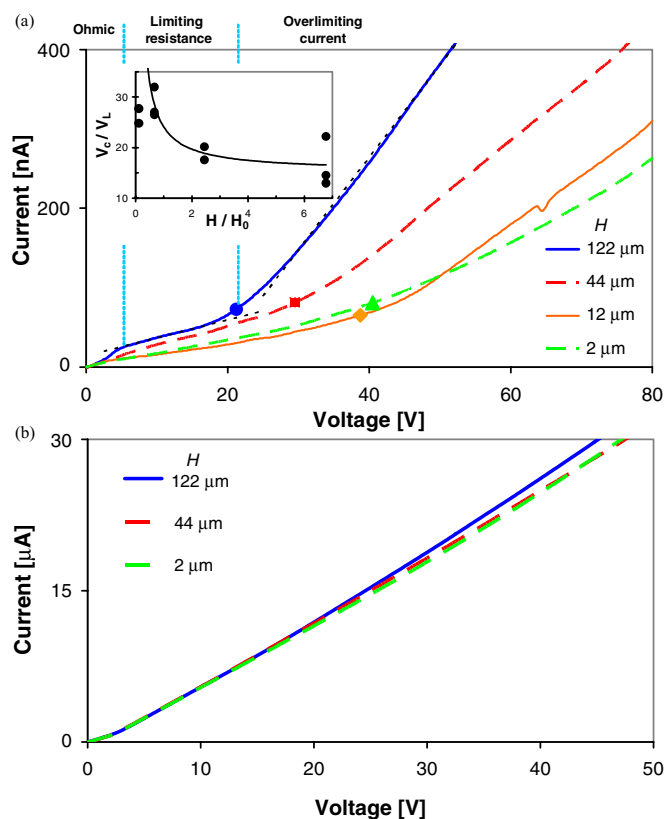


Fig. 2: (Color online) Current-voltage curves for (a) $10 \mu\text{M}$ and (b) 0.1 M KCl buffer concentrations for various microchamber depths. The inset of part (a) of the figure depicts the measured (in symbols) critical voltage (normalized by the limiting voltage V_L) for varying microchamber depths (normalized by H_0 —the threshold depth for which $L \sim d$ at 40 V applied voltage), wherein the continuous line represents the H^{-1} fit of eq. (1).

side of the nanoslot-microchamber interface, with a steady thickness that determines the CPL thickness L which, in turn, controls the overlimiting differential resistance. The CPL hence does not extend to the electrode but

saturates at a particular length due to this instability. This truncated thickness controls overlimiting ion fluxes in ion-selective membranes or electron-transfer electrodes.

How exactly the vortex instability selects L remains unknown although the electroconvection vortices are expected to suppress the diffusive propagation of the concentration polarization layer towards the electrode. Recent study [10] has established that the selected CPL thickness increases with the applied voltage. The combination of electrolyte strength (*i.e.* Debye length λ) and nanoslot depth h determines the degree of EDL overlap which, in turn, controls the ion perm-selectivity [11]. It is clear that with increased electrolyte strength, the nanoslot loses its perm-selectivity properties until eventually it behaves as a linear resistor (*i.e.* ohmic) without any CPL. It is both intuitively clear and also experimentally proven (see fig. 1(a) of [12]) that the critical voltage for the onset of the instability is reduced with increased electrolyte strength and approaches the threshold voltage for the limiting current before the loss of perm-selectivity. Another recent study [5] demonstrated the role of nanoslot entrance geometry and interchannel communication (for nanoslots of uniform depth but asymmetric transversal geometry) in controlling both the overlimiting current (current rectification) and its associated CPLs. In the case of communicating channels, the resulting selected CPL thickness was much larger than that in the non-communicating side of the nanoslot. This is in agreement with another recent paper [13] where it was shown that field focusing effects, most pronounced in the case of non-communicating narrow channels, significantly reduce the CPL length and increase the concentration gradients within it.

While all of these studies are related mainly to the effect of the nanoslot geometry, the effect of the microchamber geometry on the vortex instability selected CPL thickness and the resulting overlimiting current has not been studied. Since the electroconvection occurs outside the

nanoslot within the microchamber, it is interesting to study the effect of microchamber dimensions (particularly, its depth H in the two-dimensional geometry of fig. 1) on the selected CPL. A recent study by Jung *et al.* [14] has shown a rectification effect in the overlimiting region across a nanopore connecting asymmetric chambers. It is the different confinement constraints on the electroconvection flow within the microchambers that affected the current. However, the electric field in their microchamber varies from the predominantly tangential direction to a predominantly normal direction at the entrance of the nanopore because of field focusing [13] into the isolated nanopore. Hence, the nanopore sees both a normal field at its center that can produce an extended space charge layer SCL and a tangential field at its periphery that can impart a tangential force in the extended space charge region to produce a single vortex pair. Similar vortex pairs due to field-induced polarization have been observed at microchannel corners [15] and on curved nanoporous membranes [16]. They are not due to Rubinstein's vortex instability [17]. Another key difference is that, with the radial field lines emanating from the nanopore point source/sink, Yossifon *et al.* [13] predicted that the limiting-current voltage window vanishes and a direct ohmic to overlimiting transition occurs, which was indeed observed by Jung *et al.* [14].

In the current study, we examined the effect of the microchamber geometry on how the vortex instability selects the CPL thickness and its associated overlimiting current. For this purpose, a wide nanoslot was used (fig. 1). In contrast to the pseudo-homogenous nanoporous membrane, there is a radial field focusing into the nanoslot line sink. However, unlike the stronger point-sink of a nanopore, the field line enters the slot normally to eliminate the possibility of vortex pair formation due to field-induced polarization [15,16]. Indeed, microscopy imaging confirms that the vortex instability can indeed occur [13] for sufficiently wide nanoslots connected between two symmetric microchambers of varying depths (fig. 1).

The fabrication technique is described elsewhere [13]. However, a fabrication issue that needed to be addressed was overetching during wet-etching of the Pyrex glass with concentrated HF solution, resulting in a shorter nanoslot length with increased microchamber depth. To overcome this problem without involving different masks, a relatively long nanoslot (~ 2 mm) was used so that the maximum difference in the nanoslot lengths (associated with the deepest $122\ \mu\text{m}$ and shallowest $2\ \mu\text{m}$ microchambers) would be less than 10% (fig. 1). This discrepancy was also observed in the measured ohmic conductance.

Different dilutions of a 1 M potassium chloride (KCl) solution were used in order to change the ionic strength and control the degree of EDL overlap. Methods for measuring the I - V curves and displacing different electrolytes are also described elsewhere [13]. Based on previous experiments [13] conducted on a similar nanoslot of identical depth (190 nm) but much shorter length (0.5 mm

instead of ~ 2 mm), we chose two extreme levels of strong (0.1 M) and weak ($10\ \mu\text{M}$) electrolytes corresponding to vanishing and ideal ion perm-selectivity, respectively. In the low concentration limit, the three distinct I - V regimes are observed (fig. 2(a)): a linear ohmic region, followed by a limiting-resistance region with a small slope (large limiting differential resistance) and finally an overlimiting region. At high enough concentrations (0.1 M), only the ohmic region is observed (fig. 2(b)), irrespective of the microchamber depth. A clear indication that EDLs do not overlap within the slot and the nanochannel's perm-selectivity, space charge and non-linear I - V curve are lost—it is no longer a model for an ion-selective nanoporous membrane. Hence, under these conditions the role of the microchamber in controlling the electroconvection due to the instability vortex is lost.

In order to visualize the polarized regions, we used positive-charged rhodamine dye molecules (counterions of the nanoslot) at $10\ \mu\text{M}$ concentration. In addition, several of the tests included fluorescently tagged polymer microbeads (Duke Scientific Corporation) of $1.2\ \mu\text{m}$ in size and 0.02% volumetric concentration in order to better visualize the inner flow dynamics/structure within these depleted layers. When a large enough electric field, beyond the onset of the limiting-resistance region, is applied across the nanoslot, an enrichment region at the cathodic entrance of the nanoslot is observed with high dye concentration while a depletion region (fig. 3) is observed at the anodic side. That the depletion layer thickness L increases with the voltage for each of the microchamber depths (see fig. 3) is in agreement with previous results [10]. However, that the depletion layer increases with decreased microchamber depth for each of the applied voltages (fig. 3) was not addressed before. This suggests that geometrical restriction is less effective in suppressing the depletion region propagation. Moreover, in the case of the very shallow microchamber ($2\ \mu\text{m}$) the depletion region extended over the entire microchamber length d (fig. 1(e)), and penetrated into the drilled-hole region (figs. 3(d),(g)). An array of depletion vortices are clearly seen extending out of the microchamber-drilled hole interface. The fact that the resulting depletion regions within the drilled holes are small again is due to the fact that at these holes the geometrical restriction of the electroconvection almost vanishes. Without electroconvection to suppress the depletion layer diffusive growth, it is expected to propagate all the way to the electrodes. That electroconvection plays an important role is clearly seen in fig. 3 wherein the depletion layers inner structure consisting of a vortex pair is observed (indicated by the accumulation of colloids at the vortex pairs' stagnation points—see also linked video clips). However, no such vortices can be seen inside the shallow microchamber ($2\ \mu\text{m}$) itself (fig. 3(a)), but only at its outer boundary within the drilled-hole chamber (figs. 3(d),(g)). More conclusive evidence that the vortex instability is indeed suppressed with diminished microchamber

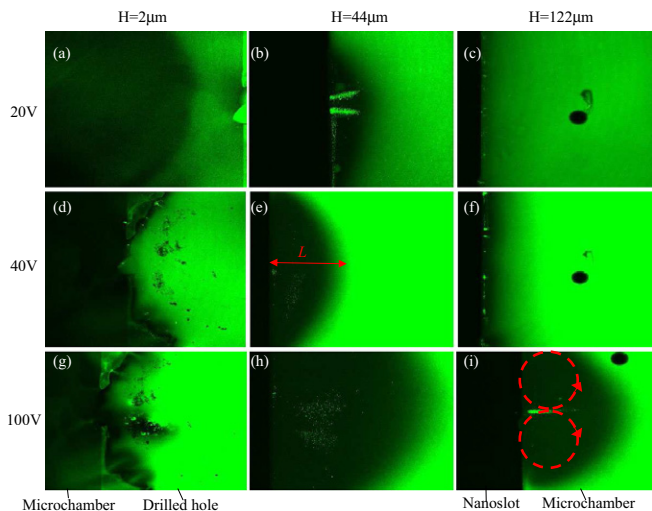


Fig. 3: (Color online) The steady-state depletion layer pattern for the various microchamber depths ($2\mu\text{m}$ —movie 1, `movie1_2um_withcolloids.mp4`, 2.6 MB MPEG-4, $44\mu\text{m}$ —movie 2, `movie2_44um_withcolloids.mp4`, 2.2 MB MPEG-4, $122\mu\text{m}$ —movie 3, `movie3_122um_withcolloids.mp4`, 2.4 MB MPEG-4) and externally applied voltage (20 V, 40 V, 100 V) combinations. Besides the rhodamine dye molecules we used fluorescently tagged colloids of $1.2\mu\text{m}$ in size for visualization purposes of the inner depletion region flow dynamics structure (see the schematic of the vortex pair). In all figures, except the $2\mu\text{m}$ —40 V and 100 V, we observe the depletion layer extending from the nanoslot into the microchamber on its anodic side. In the former cases it is the depletion layer that extends from the microchamber into the drilled hole.

depth is seen in fig. 5 below, depicting the time evolution of the depletion region upon a stepwise application of an electric field. For the deep ($122\mu\text{m}$) microchamber case an array of depletion regions appears, with each region encompassing a single vortex pair [10], which through a complex process of wavelength selection through coalescence selects a single (thicker) depletion layer and a single (larger) vortex pair. In contrast, for the case of the shallow ($2\mu\text{m}$) microchamber no such vortex pattern appears. But instead, an almost flat depletion region propagates from the nanoslot entrance over the entire microchamber until its suppression by the electro-convection vortices occurring within the reservoir just outside the microchamber. Thus, representing a stable concentration polarization layer within the chamber at steady-state conditions.

Recently, the conditions for the propagation of such concentration-polarization layers in a shallow and wide microchannel-nanochannel system were studied theoretically by Mani *et al.* and verified experimentally by Zangle *et al.* [18]. More specifically, they analyzed a constant-speed propagating front in a shallow microchannel ($1\mu\text{m}$ in height) under galvanostatic (constant-current) conditions. In their study, a shock-like concentration depletion front was observed [18] under galvanostatic conditions. We expect the same steady-state (DC) behavior

under our potentiostatic conditions (constant-voltage conditions in our current study), which differ only in the concentration-polarization dynamics (*i.e.* front velocity). The potentiostatic conditions have been shown to produce a diffusive front dynamics whose front position advances as the square root of time and whose front speed decays as the inverse square root of time [10]. Only the combined effects of axial (*i.e.* along the system length) bulk flow, electromigration and diffusion were considered in the earlier pseudo-one-dimensional model for the concentration-polarization dynamics. Such conditions are consistent with that of the current study, in the absence of any transverse electro-convective vortex instability, as observed in our shallow microchannel ($2\mu\text{m}$ in height) case (see fig. 5).

A simple scaling theory, based on the observation that the true three-dimensional electroconvection vortex instability within the microchamber can be approximated by pseudo-two-dimensional slot flow (see appendix, eq. (A.3), can capture the effects of varying the microchamber depth on the effective fluid viscosity $\eta_{eff} = 12\eta(W/H)^2$ for the two-dimensional slot flow in the vortex instability, wherein W is the nanoslot/microchamber width, H is the microchamber depth and η is the fluid viscosity. Hence, for shallower microchambers the effective viscosity is increased. Although we have focused on (hydrodynamic or Maxwell) pressure-driven hydrodynamic phenomena within the microchamber in our analysis, it is also possible that electro-osmotic flow within the nanochannel can contribute to the overall ionic transport between the connecting microchannels. Since the nanochannel depth is fixed, the latter effects are unimportant for determining the relative dependency of our device overlimiting behavior on the varying microchamber depth.

A curious observation of fig. 2(a) is the increased critical voltage for the onset of the overlimiting current with decreased microchamber depth. The critical voltage, designated by the different symbols in fig. 2(a), was determined as the voltage at which the slope (or differential conductance) reaches the rather arbitrary value of 40% of the difference between the overlimiting and limiting slopes. Other threshold values would not change the qualitative picture. This can be qualitatively explained by a theory by Rubinstein and Zaltzman [17] for the critical voltage, although obtained for a pseudo-two-dimensional homogeneous nanoporous membrane that is consistent with the two-dimensional slot flow in our microchamber geometry,

$$V_c = 8\sqrt{2\pi\eta_{eff}D/\varepsilon_0\varepsilon_f}, \quad (1)$$

wherein ε_0 is the dielectric permittivity of the vacuum, ε_f is the dielectric constant of the fluid and D is the diffusion coefficient.

Thus, combining (A.3) and (1) yields the scaling $V_c \propto H^{-1}$. The inset of fig. 2(a) shows that this scaling is in qualitative agreement with the experimental data, wherein the shallow ($2\mu\text{m}$) microchamber data point was excluded from the fitting process. This is due to the fact

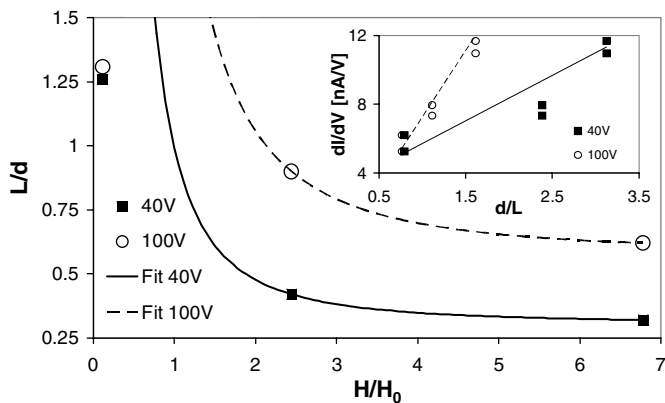


Fig. 4: Measured polarization layer lengths (L normalized by d , based on intensity profiles of the images depicted in fig. 3) for varying applied overlimiting voltages and microchamber depths (normalized by H_0). The lines represent the H^{-2} fit of eq. (3). The inset depicts the measured differential conductance (dI/dV) vs. L^{-1} , with the linear fit according to the scaling of eq. (4).

that, at such shallow microchamber depths, the concentration polarization layer propagates across the entire microchamber length d without suffering the instability and penetrates into the drilled-hole chamber (fig. 1(e)) as seen in figs. 3(d),(g). It is expected that for the shallower microchamber depths ($2\mu\text{m}$ and possibly also for $12\mu\text{m}$) the concentration polarization layer extends beyond the microchamber to a distance larger than d . Once the concentration polarization layer penetrates into the drilled-hole chamber, the microchamber loses its importance together with the dependency of the overlimiting characteristics on its depth. This might also explain the lack of observable distinction in the critical voltage between the $2\mu\text{m}$ and $12\mu\text{m}$ microchamber depths as seen in the inset of fig. 2. Herein the voltage was normalized by the limiting value (assuming ideal perm-selectivity, *i.e.* $\eta \rightarrow \infty$, for simplicity) obtained from equation (14b) of Yossifon *et al.* [12] but with the geometry and notation of the current setup,

$$V_L = -\frac{\pi}{\ln(h/L)} \frac{zRTc_0l}{2Fh \sqrt{(\Sigma/2)^2 + c_0^2}}, \quad (2)$$

wherein L is the CPL thickness, c_0 is the bulk electrolyte concentration, l is the nanoslot length, F is the Faraday number, z is the ion valency, R is the universal gas constant, T is the absolute temperature and Σ is the effective fixed volumetric charge [12]. Using the following specific values of $c_0 = 10\mu\text{M}$, $h = 190\text{nm}$, $L \sim 0.4\text{mm}$, $l \sim 2\text{mm}$, $z = 1$ and $\Sigma \sim 0.76\text{C/m}^3$ a value of $V_L \sim 1.5\text{V}$ is obtained. Furthermore, the microchamber depth was normalized by the threshold depth value H_0 (whose value is extracted from fig. 4) below which the CPL extends over the microchamber length, d .

One should note the difference between the $1/\ln(h/L)$ scaling for the limiting voltage (2) [12] and that of the $1/H$ for the overlimiting critical voltage (1). These scalings

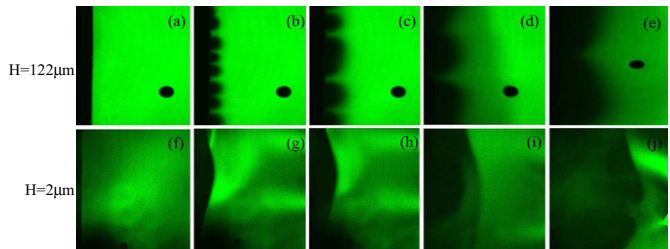


Fig. 5: (Color online) Sequence showing the depletion layer pattern evolution as a response to a step-input of 40 V. In particular, the complex process of wavelength selection by small vortices break-up through fusion and transformation into still larger vortices until a quasi-steady-like pattern is formed is clearly seen in the case of the deep ($122\mu\text{m}$ —movie 4, `movie4.122um_withoutcolloids_40V.mp4`, 0.5 MB MPEG-4) microchamber. In contrast, these patterns do not occur for the shallow ($2\mu\text{m}$ —movie 1, `movie1.2um_withcolloids.mp4`, 2.6 MB MPEG-4) microchamber. Instead, a relatively flat propagating concentration polarization layer front is observed.

are associated with field focusing [12,13] and Rubinstein's vortex instability [17] mechanisms, respectively. In the former case of underlimiting voltages (*i.e.* ohmic), it is the nanochannel geometry (in particular its depth, h) that controls the overall current. Since $H/h > 1$ for all cases, this can be described effectively as a radial field focusing from an infinite reservoir into the nanoslot irrespective of the microchamber depth H . In contrast, in the latter case of overlimiting voltages, it is the extended space charge region that controls the overall current. Hence, the field focusing effect is not important. Instead, the electro-convective processes occurring within the microchamber now becomes the rate-limiting region for the current by specifying the CPL thickness ($L/H > 1$), which in turn controls the extent of the SCL. Hence, it is the microchamber depth H that controls the instability vortex as captured in the effective viscosity.

By balancing the two counteracting forces of diffusion and electro-convection from the vortex instability for concentration polarization layer propagation, we obtain an estimate of L that scales linearly with the effective viscosity

$$L = D/u = \eta_{eff}D/(W^2\partial p/\partial x), \quad (3)$$

wherein p is the Maxwell pressure that drives the instability. Thus, combining (A.3) and (3) yields the scaling $L \propto H^{-2}$. The qualitative inverse dependency of the depletion length on the microchamber depth is clearly seen in fig. 3, while this scaling is depicted in fig. 4 for the two applied voltage levels of 40 V and 100 V. In the latter, the shallow ($2\mu\text{m}$) microchamber data point was excluded from the fitting process because its finite microchamber length d is outrun by the polarization layer, as per discussion for the fitted data in fig. 2, *i.e.* the true polarization layer length was truncated by the existence of the drilled hole. One can obtain an estimate of the critical depth for the vortex instability within the microchamber $H_0 \sim 18\mu\text{m}$ from the fitted curve at 40 V case by

stipulating that $L/d = 1$. This estimate allows us to design geometries that can suppress or enhance the instability and is consistent with the data in fig. 5. This threshold depth H_0 increases with the applied voltage, which makes intuitive sense since the CPL thickness L increases with increasing voltage (fig. 4).

Another key observation is the inverse dependency of the overlimiting differential conductance (*i.e.* slope of the overlimiting current in fig. 2(a)) on the microchamber depth, which is in qualitative agreement with Jung *et al.*'s [14] observation of the rectification current effect. This can be qualitatively explained by looking at the relationship for the overlimiting differential resistance as obtained in [12] for a wide nanoslot similar to the one in this study,

$$dI/dV = 0.75\pi WD\varepsilon_0\varepsilon_f\lambda/L, \quad (4)$$

which is inversely proportional to the CPL thickness. This scaling, $dI/dV \propto L^{-1} \propto H^2$, is indeed exhibited by the overlimiting current at both 40 V and 100 V (inset of fig. 4). That the $12\ \mu\text{m}$ behaves very similarly to the $2\ \mu\text{m}$ in terms of the critical voltage is presumably due to the fact that, in both cases, the depletion region extends across the entire microchamber into the drilled holes. Hence, it is the electro-convection outside the microchamber that controls the current. The reason that the $12\ \mu\text{m}$ has lower overlimiting differential resistance than the $2\ \mu\text{m}$ is simply due to the larger microchamber cross-section of the former case.

To summarize, we have shown that the electroconvection of a vortex instability is responsible for controlling the thickness of CPL, which specifies the overlimiting current. While in the case of sufficiently deep microchamber it is the vortex instability electroconvection that counteracts the diffusive growth of the CPL, in the shallow case the former is suppressed and the diffusive layer grows indefinitely to reach the microchamber-drilled hole interface. This understanding allows the control of not only the overlimiting current but also the critical voltage for its onset due to the vortex instability. This understanding of the fundamental mechanism should allow optimum design of high-flux ion-selective membranes and Faradaic electrodes.

GY is supported by Horev Fellow of the Taub Foundations. HCC acknowledges support from NSF-IDBR 0852741 grant. We are grateful to Prof. Y. ZHU and Prof. A. SEABAUGH of Notre Dame for the use of their equipment and for their advice.

APPENDIX

Let the x and y coordinates to be normal and tangential to the nanoslot entrance, respectively, while the z -coordinate as normal to the (x,y) -plane and in the direction of the microchamber depth. From the Poiseuille equation for the one-dimensional slot flow $\eta\partial^2u/\partial z^2 = \partial p/\partial x$, the x -component of the velocity field can be solved as

$$u = 0.5/\eta \partial p/\partial x (z^2 - (H/2)^2). \quad (A.1)$$

Averaging along the z -coordinate and writing in vector form yields

$$\vec{u} = -(1/12)H^2/\eta \vec{\nabla} p, \quad (A.2)$$

where $\vec{\nabla} = (\partial/\partial x, \partial/\partial y)$. Comparing this scaling (A.2) to that $\vec{u} \sim W^2/\eta_{eff}\vec{\nabla} p$ obtained from the Stokes equation in two-dimensions (x,y) $\eta_{eff}\nabla^2\vec{u} = \vec{\nabla} p$ yields the expression for the effective fluid viscosity

$$\eta_{eff} = 12\eta(W/H)^2. \quad (A.3)$$

REFERENCES

- [1] STEIN D. *et al.*, *Phys. Rev. Lett.*, **93** (2004) 035901.
- [2] PU Q. *et al.*, *Nano Lett.*, **4** (2004) 1099.
- [3] KIM S. J. *et al.*, *Phys. Rev. Lett.*, **99** (2007) 044501.
- [4] KARNIK R. *et al.*, *Nano Lett.*, **7** (2007) 547.
- [5] YOSSIFON G. *et al.*, *Phys. Rev. Lett.*, **103** (2009) 154502.
- [6] CHANG H.-C. and YOSSIFON G., *Biomicrofluidics*, **3** (2009) 012001.
- [7] LEVICH V. G., *Physicochemical Hydrodynamics* (Prentice-Hall, New York) 1962.
- [8] RUBINSTEIN I. and SHTILMAN L., *J. Chem. Soc., Faraday Trans. II*, **75** (1979) 231.
- [9] RUBINSTEIN S. M. *et al.*, *Phys. Rev. Lett.*, **101** (2008) 23610.
- [10] YOSSIFON G. and CHANG H.-C., *Phys. Rev. Lett.*, **101** (2008) 254501.
- [11] CHANG H.-C. and YEO L. Y., *Electrokinetically-Driven Microfluidics and Nanofluidics* (Cambridge University Press, Cambridge) 2009.
- [12] YOSSIFON G. *et al.*, *Phys. Rev. E*, **79** (2009) 046305.
- [13] YOSSIFON G. *et al.*, *Phys. Rev. E*, **81** (2010) 046301.
- [14] JUNG J.-Y. *et al.*, *Anal. Chem.*, **81** (2009) 3128.
- [15] THAMIDA S. K. and CHANG H.-C., *Phys. Fluids*, **14** (2002) 4315; YOSSIFON G. *et al.*, *Phys. Fluids*, **18** (2006) 117108.
- [16] DUKHIN S. S., *Adv. Colloid Interface Sci.*, **35** (1991) 173.
- [17] RUBINSTEIN I. and ZALTZMAN B., *Phys. Rev. E*, **62** (2000) 2.
- [18] MANI A., ZANGLE T. A. and SANTIAGO J. G., *Langmuir*, **25** (2009) 3898; ZANGLE T. A., MANI A. and SANTIAGO J. G., *Langmuir*, **25** (2009) 3909.